

<https://doi.org/10.1038/s43247-024-01726-8>

# Characteristics and drivers of marine heatwaves in the western South Atlantic

**Camila Artana** <sup>1,2</sup>, **Regina R. Rodrigues** <sup>3</sup>, **Juliette Fevrier** <sup>1</sup> & **Marta Coll** <sup>2</sup>

Marine heatwaves are events of extreme warming in the ocean and have devastating consequences for marine life. Here we used a K-mean clustering analysis to detect different types of marine heatwaves along the South American coast from 10°S to 45°S and identify their remote drivers. In the central part of the domain, marine heatwaves are associated with atmospheric blocking caused by wave trains triggered by the Madden-Julian Oscillation. On the other hand, marine heatwaves occurring along the northern and southern coast of South America are associated with El Niño and La Niña events, respectively. The intensity and duration of these marine heatwaves are modulated by the development phase and intensity of the Niño and Niña events. By identifying the climatic modes of variability leading to each type of marine heatwaves, our study can help develop adaptation strategies, such as early warning systems, to prevent the devastating effects of marine heatwaves.

The ocean absorbs around 89% of the excess heat generated by human-induced greenhouse gas emissions<sup>1</sup>, and as a consequence, extreme events of ocean warming called Marine Heatwaves (MHWs) are becoming more frequent and intense globally<sup>2</sup>. Even though trends in ocean warming during the last decades are positive in almost all the world's oceans, there are hotspots of warming in highly biologically productive areas. The western South Atlantic, spanning from 10°S to 45°S, is one of these hotspots, with trends in sea surface temperature (SST) surpassing 0.3 °C per decade in some regions (Fig. 1).

Regions of extreme warming are expected to present a high occurrence of MHWs as well<sup>3</sup>. These events have devastating consequences for marine ecosystems ranging from habitat shifts and changes in population structure to high mortality of various marine species<sup>4</sup>. Specifically for the western South Atlantic, MHWs have been reported to impact primary productivity, yellow clams and corals<sup>5,8</sup>.

MHWs have different drivers. They can be locally generated either by air-sea fluxes or ocean dynamics and remotely by modes of climate variability, such as El Niño Southern Oscillation (ENSO)<sup>9</sup>. For the western South Atlantic between 20°S and 30°S, Rodrigues et al.<sup>6</sup> showed that atmospheric blocking, associated with high-pressure centres, inhibits cloud formation over the region, increasing shortwave radiation into the ocean. Together with weaker winds that reduce evaporative cooling, atmospheric blocking leads to MHWs in the region during austral summer. In turn, the atmospheric blocking is remotely driven by the Madden-Julian Oscillation associated with deep convection over the Indian Ocean. Later, Sen Gupta et al.<sup>10</sup> showed that a large fraction of the most extreme MHWs in the subtropical oceans are associated with persistent atmospheric high-pressure systems and weakened surface winds, similar to the western South Atlantic.

Ocean heat advection can be important for driving MHWs along the Brazil Current. Goes et al.<sup>11</sup> showed that a westward propagating oceanic feature with a periodicity of 3–5 years modulates the interannual variability of MHWs in the western South Atlantic. In the Brazil–Malvinas confluence region, an increase in the eddy activity associated with the Brazil Current extension can enhance warming over the region, leading to MHWs<sup>12,13</sup>. More generally, mesoscale eddies have been identified as a relevant feature involved in the development and dissipation of MHWs across various western boundary regions<sup>14</sup>.

Despite the existing studies on the western South Atlantic, a comprehensive characterisation of the MHWs along the South American coast is still lacking. Quantifying MHW characteristics is key for the establishment of connections between these events and their effects on marine ecosystems<sup>4,15,16</sup>. Moreover, such MHWs characterisation and systematic analysis are necessary to improve their short-term (seasonal) prediction and long-term projections under climate change, as the occurrence of MHWs has increased in this region over the past decades and will continue to do so in the future<sup>6,17</sup>. For this reason, the main objective of this study is to characterize MHWs along the coast of South America between 10°S and 45°S by applying cluster analysis to the Mercator Ocean High Resolution (1/12°) Ocean reanalysis (GLORYS12) for the period of 1993–2019. We will show that the different types of MHWs identified by the cluster analysis are associated with different modes of climate variability.

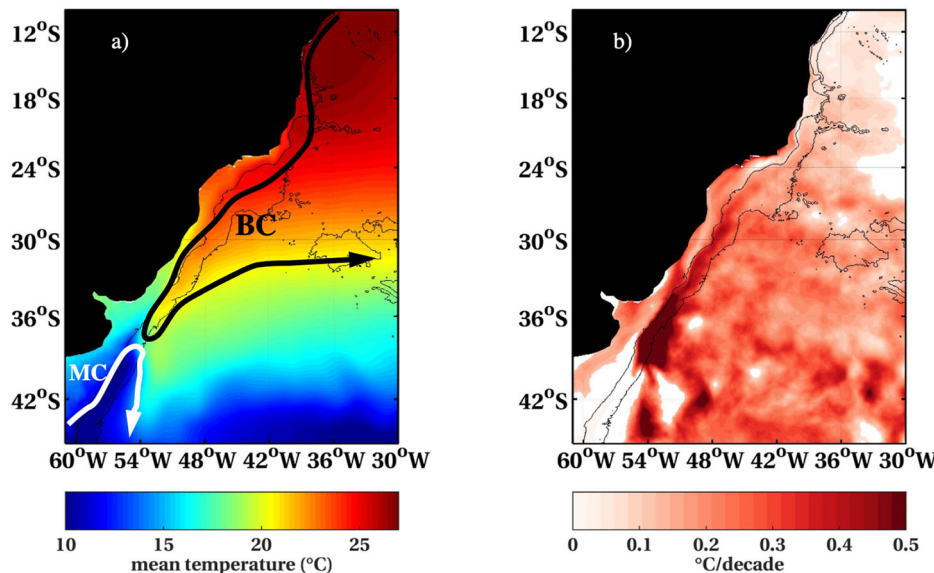
## Results

### Marine heatwaves characteristics in the western South Atlantic

The characteristics of MHWs along the western South Atlantic coast vary considerably with latitude (Fig. 2). In the northern domain, MHW events

<sup>1</sup>Laboratoire LOCEAN-IPSL, Sorbonne Université, (UPMC, Université Paris 6), CNRS, IRD, MNHN, Paris, France. <sup>2</sup>Institute of Marine Science (ICM)-CSIC, Barcelona, Spain. <sup>3</sup>Department of Oceanography, Federal University of Santa Catarina, Florianópolis, Brazil. e-mail: [cartlod@locean-ipsl.upmc.fr](mailto:cartlod@locean-ipsl.upmc.fr)

**Fig. 1 | Sea surface temperature in the western South Atlantic.** **a** Mean sea surface temperature (in °C) and **b** sea surface temperature trends (in °C decade<sup>-1</sup>) computed from GLORYS12 reanalysis for the period of 1993–2019. Only values statistically significant at the 95% confidence interval using a Mann–Kendall test are plotted. BC stands for Brazil Current and MC for Malvinas Current. The 300 m and 3000 m isobaths are indicated with black contours.



occur on average 1.5 times a year with a mean duration of 30 days, mean intensity of 0.7 °C and maximum intensity of 0.9 °C (circles in Fig. 2b–e), whereas in the central domain, they occur on average 2 times a year with a mean duration of 17 days, mean intensity of 1.5 °C and maximum intensity of 2 °C (squares in Fig. 2b–e) and in the southern domain they occur on average 3 times a year with a mean duration of 10 days, mean intensity of 4 °C and maximum intensity of 7 to 10 °C (stars in Fig. 2b–e).

Note that the frequency of MHWs can be considered in terms of the number of MHW days per year (Fig. 2a). In this case, the northern domain is exposed to a higher number of MHW days. Moreover, the longest events (lasting more than 5 months) are exclusively observed in the northern domain (Fig. 2g), and the most intense events (reaching more than 10 °C) are found in the southern region (along the Brazil–Malvinas Confluence) between 35°S and 45°S (Fig. 2g). Therefore, from the northern to the southern domains, MHW events become more frequent and stronger but less persistent (Fig. 2g). For this reason, higher values of cumulative intensity, which accounts for both frequency and intensity, are found in the southern region (Fig. 2f). In summary, the northern domain is dominated by longer and weaker MHWs and the southern domain by shorter and more intense MHWs, whereas the central domain has middle of the range characteristics (Fig. 2g). It is worth noting that the same spatial distribution in the MHW characteristics is observed when the trend is removed from the SST maps (Supplementary Fig. 1).

In order to separate the different MHWs into groups according to their characteristics, we applied a K-mean clustering analysis (see methods for more details). The clustering identified seven different groups for the studied region (Fig. 2h). Each group is constrained to a particular geographical region (white colours in Fig. 3 indicate that the group is never active in those regions). Groups 1 and 2 comprise MHWs from the northern part of the study area (Fig. 3a, b, h, i). These episodes are not very intense (mean of 1 °C). Group 1 selects extremely long-lasting heatwaves (mean duration of 50 to 70 days), while Group 2 gathers shorter ones (mean duration around 10 days). Groups 3 and 4 encompass MHWs from the central region of the study area. MHWs belonging to this group show a low to moderate mean intensity (1–2 °C) (Fig. 3c, d, j, k). MHWs from Group 3 are on average short in duration, while those from Group 4 are longer (30 days). Lastly, Groups 5, 6, and 7 select MHWs in the southern part of the study region, in the vicinity of the Brazil–Malvinas Confluence (Fig. 3e–g, l, m, n). The MHWs range from high to extreme intensity (mean of 2–5 °C) and vary in duration (mean of 5 to 15 days).

We then explored the seasonality of the MHWs belonging to each group. Figure 4 shows the total number of event days that occur each month

for each group over the entire period. Certain clusters identify episodes that are more common during a given season. For example, there is a larger number of MHWs occurring in austral summer for Groups 1, 4, 6 and 7. Groups 1 and 7, with 87 and 13 events respectively, have their peak in March. Groups 4 and 6 peak, with respectively 61 and 6 events, have their peak in February. Group 1, with 77 events, also has a secondary peak in May. Group 5 with 15 events peaks predominantly in winter (August). Group 2 shows an increase in the number of events during fall and spring.

In Table 1, we provide a summary of the MHW characteristics inferred from this section. The different “flavours” of MHWs could indicate different drivers at play. These MHW drivers will be investigated in the following section.

#### Drivers for each type of MHWs

To identify the different drivers for each group, we computed monthly time series considering the percentage of pixels from the total that corresponds to each group (Fig. 5). Interestingly, Groups 1 and 4, associated with longer-lasting MHWs, present larger peaks in their time series in the last decade, while Groups 2 and 3, which select shorter MHWs, present more intense peaks at the beginning of the time series.

Since ENSO is an important mode of climate variability impacting the western South Atlantic and eastern South America<sup>18–20</sup>, we computed the correlation between the time series and ENSO index (Tab. 1). We find a particularly large and positive correlation between Group 1 and 2 and negative correlation with Groups 5, 6 and 7. This suggests that El Niño plays a role in developing long-lasting MHWs located in the northern region, while La Niña is important for developing intense MHWs in the southern region.

To gain some understanding of the connection between ENSO and MHWs, we calculated composites of SST anomalies for each group (Fig. 6) by selecting the dates in which the time series of MHW pixel percentage exceeds two standard deviations (black line in Fig. 5). Groups 1 and 2 appear to be linked to warm SSTs in the equatorial Pacific. Specifically, SST composites indicate that summer MHWs from Group 1 correspond to well-developed El Niños, while MHWs from Group 2 are associated with either the onset or decay phases of El Niño events. Significant and positive SST anomalies are also observed in the Indian Ocean and in the South Pacific for the composites of MHWs from Group 1. These patterns correspond to the classic SST anomalies observed during El Niño<sup>21</sup>. In contrast, Groups 3 and 4 do not exhibit any particular relationship with Pacific SSTs. Finally, Groups 6 and 7 are linked to La Niña events (cold anomalies in the equatorial Pacific). Negative SST anomalies in the equatorial Pacific are particularly strong for Group 7. In contrast, winter MHWs from Group 5 are linked to

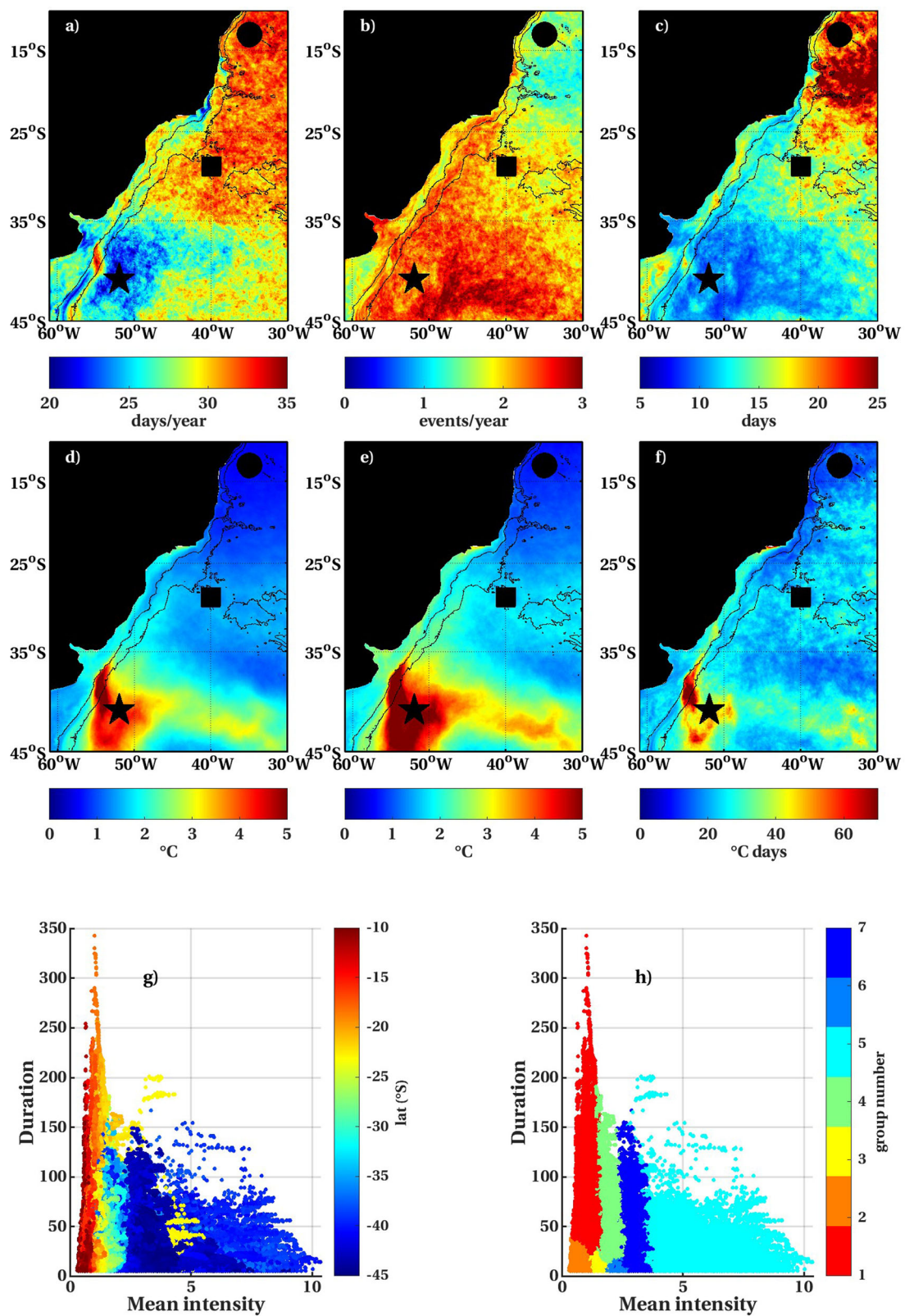


**Fig. 2 | MHW characteristics in the western South Atlantic from GLORYS12 reanalysis.** **a** Frequency (days year<sup>-1</sup>); **b** frequency (events year<sup>-1</sup>); **c** duration (days); **d** mean intensity (°C); **e** maximum intensity (°C); **f** cumulative intensity (°C day). Circles, squares and stars indicate the position where the characteristics are

described in the text. **g** Scatter plot of MHWs intensity (°C) vs MHWs duration (days) with colours indicating the latitude. **h** Same as **g** with colours indicating the group number obtained from the cluster analysis.

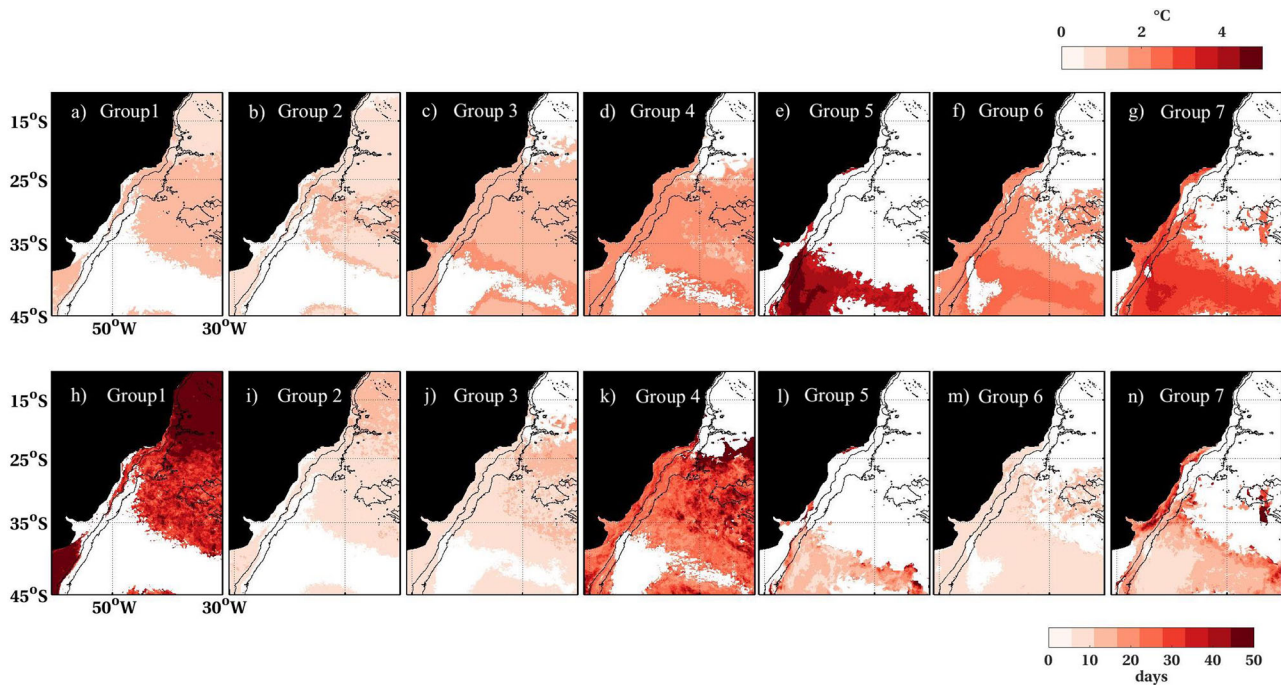


Fig. 3 | MHWs characteristics by groups. a–g MHWs mean intensity for Groups 1–7, respectively. h–n MHW mean duration for Groups 1–7, respectively.

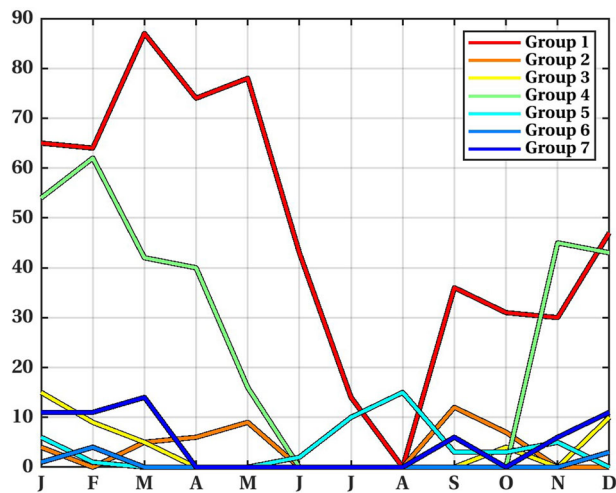


Fig. 4 | MHWs seasonality by groups. Total number of event days that occur for each month over the entire period. Event days were considered if MHWs for each day exceeded a spatial coverage larger than 10%.

weak cold SST anomalies in the equatorial Pacific, probably associated with either the onset or the decay phases of La Niña events (Fig. 6).

It is worth noting that the monthly record used here is relatively short, which probably explains the lack of significance for certain composite values. However, the composite maps suggest that the intensity of El Niño and La Niña events modulates the intensity and duration of MHWs in the northern part and southern part of the study region, respectively. Furthermore, the SST composites comprising the entire Southern Ocean provide a broader spatial context to the MHWs occurring along the western South Atlantic. In fact, the SST composite also reveals that MHWs from Group 5 are confined to the Brazil–Malvinas Confluence, whereas Groups 6 and 7 are linked to positive anomalies extending further south of the study area, affecting the entire Argentine Basin as well. Indeed, the SST composite from Group 7 resembles the positive phase of the South Atlantic Dipole mode (Fig. 6). This is consistent with Rodrigues et al.<sup>19</sup>, who showed that La

Niña events are associated with positive South Atlantic dipole events and thus warming over the southern region.

Detrended SST composites yield similar spatial patterns to those described above (Supplementary Fig. 2).

To identify the remote drivers and their teleconnection to the South Atlantic responsible for each type of MHW, we analysed composites of geopotential height anomalies in the upper troposphere at 200 hPa (Fig. 7). The composites reveal distinct patterns: Groups 1 and 2 exhibit a connection with a wave pattern originating in the central equatorial Pacific, closely resembling the ENSO-induced Pacific–South American teleconnection pattern (PSA2). In the Southern Hemisphere, this teleconnection corresponds to the third leading pattern of atmospheric variability<sup>22–24</sup>. In agreement with Rodrigues et al.<sup>19</sup>, we observe that the PSA2 influences the South Atlantic temperatures through the establishment of a persistent high-pressure system (not shown) forced by strong positive anomalies of geopotential height at 200 hPa (Fig. 7a, b).

Groups 3 and 4 patterns near the South Atlantic closely resemble those documented in Rodrigues et al.<sup>6</sup>. As shown by these authors, Rossby wave trains that originate in the Indian Ocean generally travel with the atmospheric jet up to the western South Atlantic and generate a positive anomaly of geopotential height over the central region. The latter leads to

Table 1 | Summary of MHWs characteristics for each group and correlation coefficient (R) between group time series and ENSO index (El Niño–Southern Oscillation)

Group	Region	Intensity	Duration	Peak season	R (ENSO)
1	Northern	Weak	Long	Summer and fall	0.48
2	Northern	Weak	Short	Fall and spring	0.24
3	Central	Weak	Short	Summer	–
4	Central	Moderate	Long	Summer	–
5	Southern	Very intense	Short	Winter	–0.19
6	Southern	Moderate	Short	Summer	–0.34
7	Southern	Intense	Short	Summer	–0.38

Only statistically significant values at the 95% confidence level are shown.

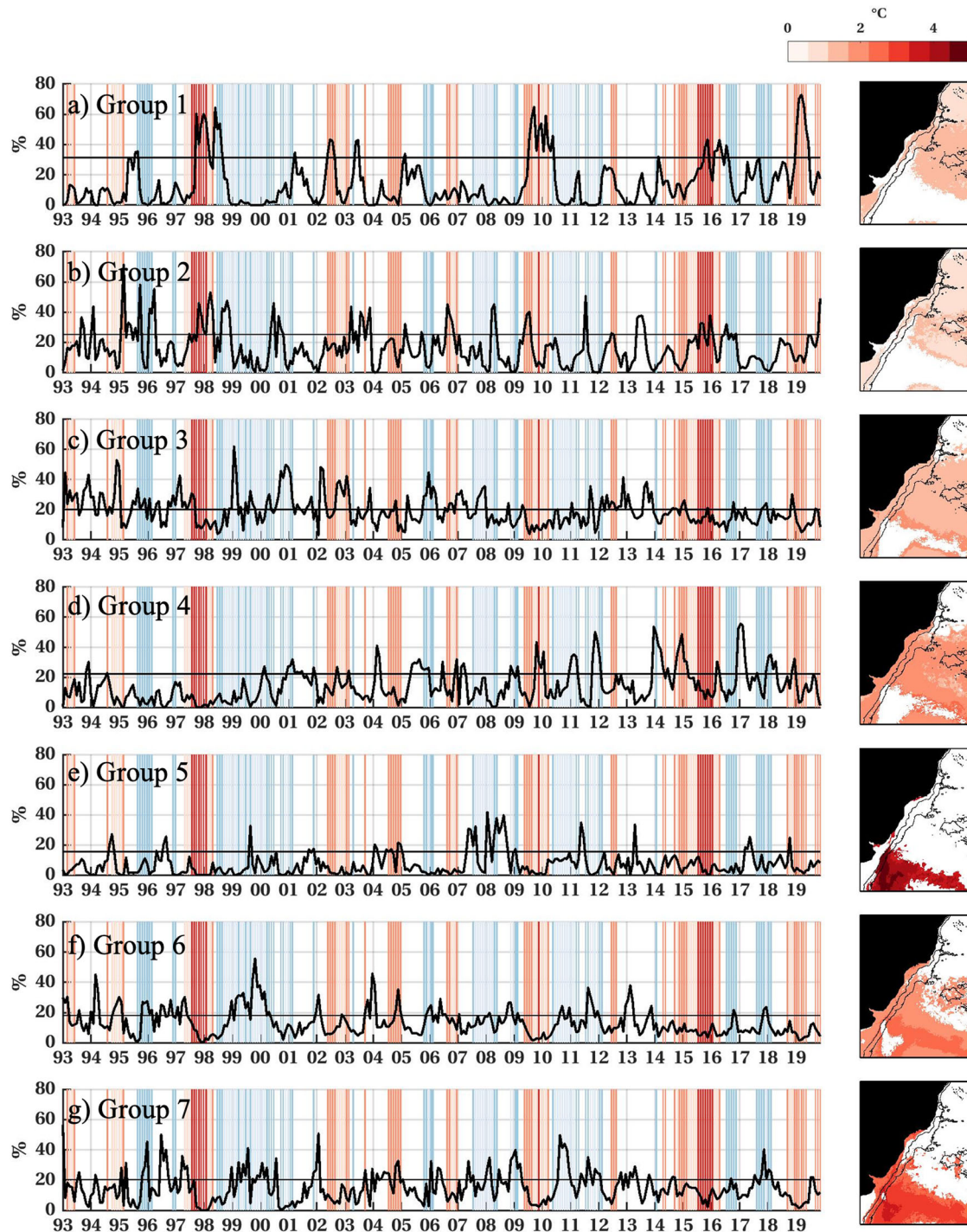


**Fig. 5 | Contribution of each group for the MHWs over the study area.** Monthly time series of the percentage of pixels for each group contributing to the total number of pixels with MHWs in the whole domain. The positive and negative phases of

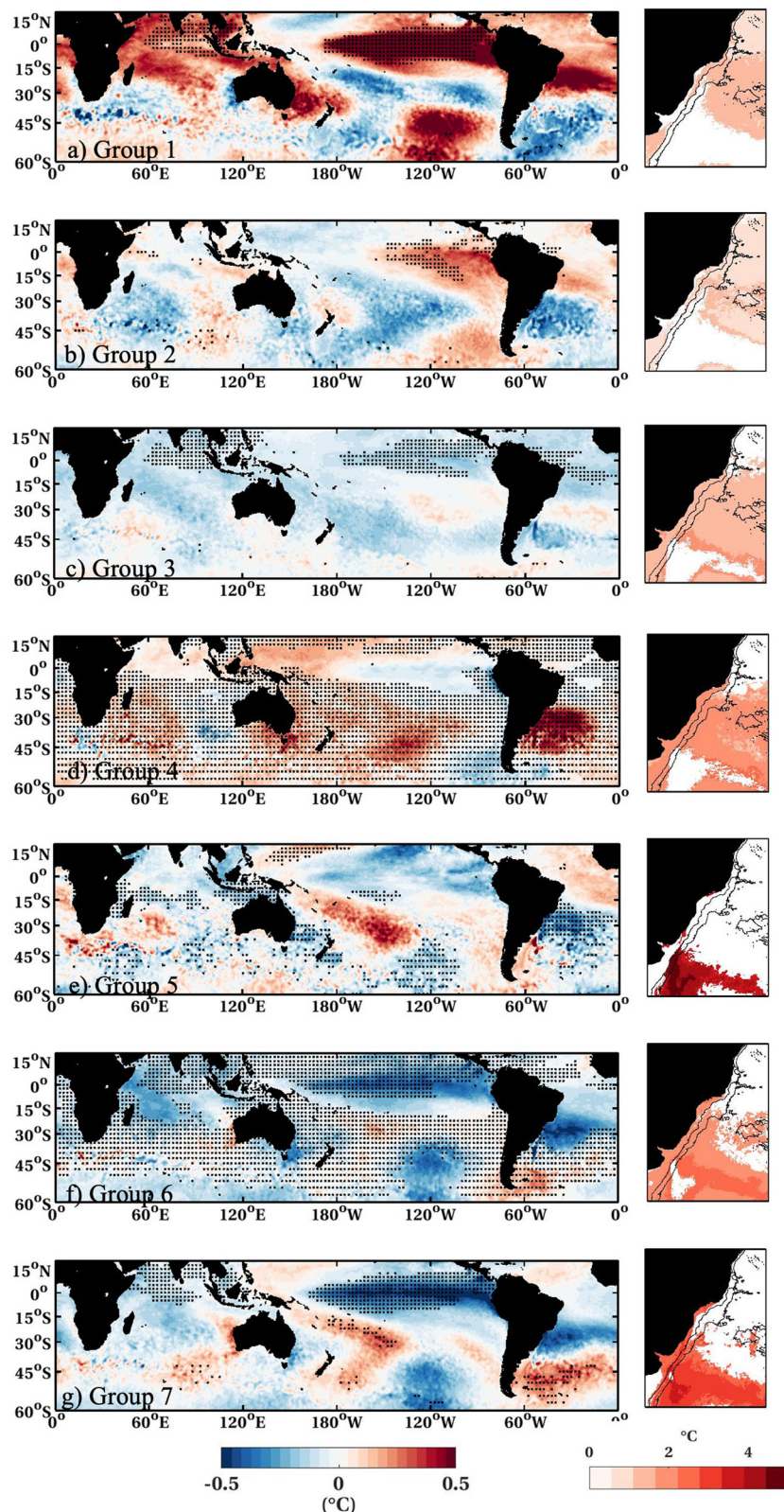
ENSO are indicated by red and blue stripes, respectively. The black straight lines represent 2 standard deviations. Panels on the right indicate the intensity of the MHWs for each group, as in Fig. 3a-g.

atmospheric blocking over the region, suppressing the South Atlantic Convergence Zone, its associated convection and clouds, leading to more shortwave radiation into the ocean and, thus, MHWs. This wave pattern is associated with the Madden-Julian Oscillation (MJO), which triggers atmospheric blocking that contributes to the onset of MHWs in the central part of the study area. Indeed, the composites of outgoing longwave radiation (OLR) for Groups 3 and 4 show a pattern very similar to phase 2 of the MJO, which is associated with enhanced convection in the eastern Indian Ocean (negative values of OLR in Supplementary Fig. 3). Moreover, the MJO is active during 93 and 94% of MHWs from Group 3 and Group 4,

respectively (c.f. methodology, section 4.7). Negative OLR anomalies over the Indian Ocean are larger in composites from Group 4 than those in Group 3. This is consistent with larger geopotential height anomalies over the central region associated with Group 4 (Fig. 7). The wave train associated with Group 4 is more developed and presents larger geopotential anomalies than those from Group 3, suggesting that the intensity and phase of the MJO modulates the MHWs intensity and duration in the central part of the study area.

Finally, Groups 5, 6, and 7 are associated with a wave train pattern originating in the equatorial Pacific associated with La Niña events that

**Fig. 6 | Large-scale SST patterns associated with each MHW group.** Composite of SST anomalies for each MHW group (see Methods for more details). The black dots indicate regions where composites are statistically significant at the 95% confidence level. The right panels indicate the intensity of the MHWs for each group, as in Fig. 3a–g.



results in a high-pressure system located to the south that probably drives the development of MHWs in the vicinity of the Brazil–Malvinas Confluence. The wave pattern for Group 5 is distorted in the zonal direction, and geopotential height anomalies are relatively low as the associated MHWs occur during winter when La Niña events are weak in their onset or decay phases. Notably, this group, which is linked to MHWs confined to the Brazil

Malvinas Confluence region (as shown in Fig. 6e), is associated with a localised anticyclonic circulation that results in northerly winds capable of inducing a southward displacement of the Subtropical Front and thus the confluence region allowing warmer waters from the Brazil Current to reach further south (Supplementary Fig. 4). The composite of the wind stress curl anomalies for Group 5 (Supplementary Fig. 4b) shows large positive values

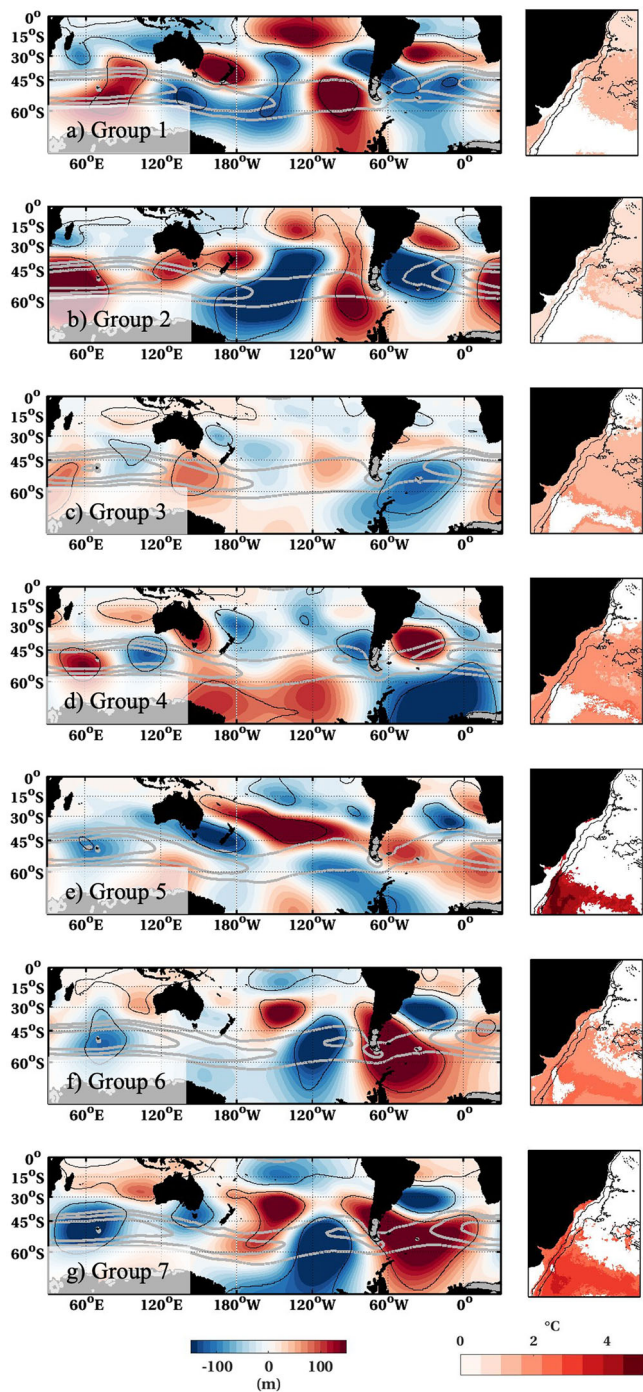


**Fig. 7 | Large-scale atmospheric patterns associated with each MHW group.** Composite of geopotential height anomalies at 200 hPa for each MHW group. Geopotential height anomalies at 200 hPa are represented in colour shading (in m) and zonal wind at 850 hPa in grey solid contours (in  $\text{m s}^{-1}$ ). The contour intervals are  $5 \text{ m s}^{-1}$ , starting at  $20 \text{ m s}^{-1}$ . The black contours delimit regions where composites are statistically significant at the 95% confidence level. The right panels indicate the intensity of the MHWs for each group, as in Fig. 3a–g.

along the Subtropical Front (southern edge of the subtropical gyre) associated with an intensification and southward displacement of the South Atlantic subtropical high (anticlockwise atmospheric circulation in Supplementary Fig. 4a). This leads to a more intense Brazil Current advecting warm waters to the south, and thus a southward displacement of the confluence region and more eddy activity, generating the MHWs there (Supplementary Fig. 4c). The corresponding persistent atmospheric high

systems for each group probably responsible for the development of the MHWs are located in regions where the low level jet slows down (grey solid contours in Fig. 7), and the wave trains tend to veer (e.g. refs. 25–27).

In summary, the intensity and duration of MHWs from Groups 3 and 4 are modulated by the MJO phase and corresponding intensity, while those of Groups 1 and 2 and those from Groups 5, 6, and 7 seem to be modulated by the development phase and the intensity of El Niños and La Niñas, respectively. As such, the correlations between the group time series are negative for Groups 1–2 associated with El Niños against Groups 5–7 associated with La Niñas, are positive between Groups 5–6 and Group 7, all associated with La Niñas, and not significant against Groups 3 and 4 that are driven by MJO (Supplementary Table 1).

## Discussion

This study provides a comprehensive characterisation of MHWs along the Brazilian Coast, encompassing their properties and underlying physical drivers. In agreement with findings from Rodrigues et al.<sup>6</sup>, we observed that MHWs occurring in the central part of the domain are primarily driven by atmospheric blocking events associated with the Madden-Julian Oscillation. In contrast, MHWs occurring in the northern and southern areas are linked respectively to El Niño and La Niña events, through atmospheric teleconnection patterns that lead to the development of persistent high-pressure systems. Furthermore, we observed that the intensity and duration of MHWs are modulated by the intensity and duration of El Niño and La Niña events.

Our analysis links local extremes with remote drivers and large-scale climate modes of variability following an “inside-out” approach (as defined by Chapman et al.<sup>28</sup>). First, MHWs were detected and then large-scale drivers were identified. However, we did not investigate the local drivers. Recently, an outside-in approach has been proposed by Chapman et al.<sup>28</sup>. In this methodology the authors identify first large-scale patterns associated with extreme SST by employing an Archetype analysis to go from global to local scales. This methodology allows distinguishing events driven by large-scale modes of climate variability and those dominated by local processes. Local processes certainly play an important role in maintaining the MHWs once they have been triggered. This could be particularly the case for MHWs belonging to Group 4, which are long-lasting (>30 days) and seem to be triggered by the MJO which only lasts a few weeks. As a result, composite maps may include days when the MJO is not active. This probably explains why the MJO Rossby waves associated with Group 3 and 4 are not as distinct as those identified in Rodrigues et al.<sup>6</sup>. Similarly, Group 5 corresponds to winter MHWs highly localized to the Brazil–Malvinas Confluence. Although the composite maps show negative SST anomalies over the equatorial Pacific, the anomalies are relatively weak. This is in agreement with the wave train observed in the geopotential height composite, which is also relatively weak and distorted in the zonal direction. This is consistent with the fact that austral winter is either the onset or decay phase of ENSO. Moreover, the impacts of ENSO teleconnection can be more intense in other seasons rather than the mature season (austral summer). Our interpretation is then that seasonal phase lock with local factors might contribute to the development of this type of event, such as intense eddy activity at the confluence or frontal displacements of the subtropical front. Finally, we did not investigate other processes that can lead to a time lag between the more rapidly remote atmospheric forcing and the slower ocean response that can set favourable conditions for the development of MHWs. For instance, Morrow et al.<sup>29</sup>, showed that changes in winds near the Southern Ocean can increase eddy activity 2–3 years later, subsequently impacting SST along the Southern Ocean fronts. Recently, Goes et al.<sup>11</sup>, showed that large-scale ocean circulation at interannual time scales (an oceanic westward propagating mode with 3–5 years of periodicity) may set a baseline for temperature extremes or interact with these events.

Given that ENSO and MJO provide a certain degree of predictability, our findings linking each type of MHW to specific modes of climate variability lay the foundation for MHW forecasting and the development of strategies such as early warning systems to mitigate the dramatic impacts of

MHWs on ecosystems. For example, the southernmost reefs located in the region influenced by Group 1 (17°S), have been historically spared from ocean warming due to turbid waters reducing solar irradiance. However, they experienced an unprecedented MHW in 2019 that caused a catastrophic decline in coral cover<sup>8</sup>. From December 2018, the ENSO index was significantly high (0.7), and five months later, Group 1 showed a record peak in April 2019. Another example is the 2017 MHW, one of the most extreme in the western South Atlantic in the region<sup>30</sup> associated with Group 4, which led to mass mortality of yellow clams, devastating populations across Uruguay, Argentina, and Brazil. This event also triggered toxic algal blooms, leading to the closure of recreational beaches. From January to March 2017, the MJO was particularly active, and the Group 4 time series peaked in February 2017. These two cases illustrate the societal relevance of our study. A precise knowledge of the relationship between ENSO, MJO, and MHWs at that time could have helped to anticipate the most vulnerable regions and potential intensity of the MHWs. Establishing connections between MHW characteristics and their biological impacts is essential for addressing the devastating effects of such events. Future research should focus on linking MHW typologies with ecological and socioeconomic changes to help predict future potential effects.

## Methods

### Satellite sea surface temperature

The daily SST data used were obtained from the National Oceanic and Atmospheric Administration Optimum Interpolation Sea Surface Temperature (NOAA OISST V2.1<sup>31</sup>). The data are freely available on the NOAA website <https://www.ncei.noaa.gov/data/sea-surface-temperature-optimum-interpolation/v2.1/access/avhrr/>. This data set is an interpolation of remotely sensed SSTs from the Advanced Very High-Resolution Radiometer (AVHRR) imagery into a regular grid of 0.25 and daily temporal resolution from 1981 to the present.

### Atmospheric reanalysis

Monthly atmospheric fields were obtained from the fifth-generation ECMWF reanalysis (ERA5<sup>32</sup>). ERA5 has a spatial resolution of 0.25° and covers the period 1940 to present. This atmospheric reanalysis combines in situ observations in a model simulation to produce an atmospheric state.

We also used monthly data of interpolated outgoing longwave radiation (OLR) with a spatial resolution of 2.5° for the period 1993–2019 (<https://psl.noaa.gov/data/gridded/>). The OLR MJO index was obtained from the Australian Government Bureau of Meteorology (<http://www.bom.gov.au/climate/mjo/>).

### ENSO index

We used the detrended ENSO index (Niño 3.4) available at [https://origin.cpc.ncep.noaa.gov/products/analysis\\_monitoring/ensostuff/ONI\\_v5.php](https://origin.cpc.ncep.noaa.gov/products/analysis_monitoring/ensostuff/ONI_v5.php). El Niño or La Niña events are defined when the Niño 3.4 SSTs exceed  $\pm 0.5^{\circ}\text{C}$  for a period of at least 6 consecutive months.

### Ocean reanalysis

We used daily means of high-resolution (1/12°) global Mercator Ocean reanalysis for the period of 1993–2020 (hereafter, GLORYS12) from Copernicus Marine Environment Monitoring Service (CMEMS, <http://marine.copernicus.eu/>)<sup>33</sup>. GLORYS12 reanalysis uses the reprocessed atmospheric forcing coming from the global atmospheric reanalysis ERA5 and benefits from a few changes in the system settings about observation errors. The reanalysis has 50 vertical levels with 22 levels in the upper 100 m, leading to a vertical resolution of 1 m in the upper levels and 450 m at 5000 m depth. The physical component of the reanalysis is the Nucleus for European Modeling of the Ocean platform (NEMO). The reanalysis assimilates observations using a reduced-order Kalman filter with a 3-D multivariate modal decomposition of the background error and a 7-days assimilation cycle<sup>34</sup>. Along-track satellite altimetric data from CMEMS<sup>35</sup>, satellite sea surface temperature from NOAA, sea-ice concentration, and in situ temperature and salinity vertical profiles from the latest CORA in situ

databases<sup>36,37</sup> are jointly assimilated. A 3D-VAR scheme provides an additional 3-D correction for the slowly evolving large-scale biases in temperature and salinity when enough observations are available<sup>34,38</sup>. The high-resolution ocean reanalysis (8 km) has been extensively validated against existing observations in the region<sup>39–41</sup> and has shown good skill in reproducing the front locations (in particular the Brazil–Malvinas Confluence) as well as the high mesoscale eddy activity in the region. Moreover, it has been widely used in other regions of the ocean to study MHWs (e.g. refs. 42–44).

The surface MHWs are well reproduced in the reanalysis in terms of amplitude, frequency and duration (Supplementary Fig. 5). The reanalysis MHW intensity is larger by about 1 °C compared to the satellite MHWs intensity at the Confluence region. The reanalysis presents more frequent MHWs south of 24°S compared to satellite-detected MHWs (3 MHWs per year against 2) and less frequent events north of 24°S (1 per year compared to 2). The mean duration of the MHWs is larger in the reanalysis than in the satellite data by about 10 days to the north of 24°S. The discrepancies between the reanalysis-detected MHWs and the satellite-detected MHWs may be due to the spatial resolution of each product (1/12° vs 1/4°). The interpolation involved in the satellite product due to cloud coverage can also lead to the observed differences between the satellite and the reanalysis. The interpolation artefacts can be somehow smoothed in the reanalysis as satellite altimetry data is also assimilated (which is not influenced by cloud coverage). The integrated nature of the reanalysis, combining satellites and in situ observations with the model dynamics, does not guarantee that all SST information is retained. Overall MHWs metrics from satellite and reanalysis are in good agreement.

### MHW detection

Here, we considered the definition proposed by Hobday et al.<sup>45</sup>, in which MHWs are prolonged and discrete events during which the water temperature is anomalously warm, with temperatures exceeding the seasonally varying 90<sup>th</sup> percentile for more than five days. This definition has been implemented to each grid point using a freely available software tool in Matlab<sup>46</sup>.

We then computed a set of properties, including frequency, duration, mean maximum and cumulative intensity and number of MHWs per year<sup>45</sup>. These metrics are defined as follows: “mean (maximum) intensity” is the mean (maximum) temperature anomaly, measured relative to the climatological seasonally varying mean, during the event and “cumulative intensity” is the integrated temperature anomaly. “Duration” is the number of days between the event’s start and end dates.

### Clustering method

We used the k-means clustering method<sup>47</sup> to classify MHWs detected from the ocean reanalysis (1/12°) in different groups based on common characteristics. We used mean, maximum, cumulative intensity and duration as variables for the clustering algorithm. The k-means algorithm is an iterative method. The obtained distribution did not change among different initialisations, confirming the robustness of our results. We used a correlation-based method to determine a suitable number of clusters. We applied the kmean method to the GLORYS12 SST considering k values (groups) ranging from 2 to 12. For each k, the algorithm partitioned the data into k clusters. For each k, we computed the mean of each cluster and created two vectors: The first vector contained the original data points, the second vector contained the mean values of the corresponding clusters. We then calculated the correlation between these two vectors. This correlation measures how well the cluster means represent the original data points. As the number of clusters k increases, the correlation between the vectors also increases. When k equals the number of data points, each cluster contains a single data point, resulting in a perfect correlation of 1. The optimal number of clusters is identified at the point where the correlation stabilizes, even if more clusters are added. This indicates that increasing the number of clusters beyond this point does not improve the representation of the data. In our case, the correlation tended to a constant when considering 7 groups.

## Composite analysis

Composite maps of SST, geopotential height at 200 hPa and OLR were built by averaging the monthly maps corresponding to the dates on which the group time series showed values larger than two standard deviations in Fig. 3. The statistical significance of the composites is evaluated using a T-student test at the 95% confidence level. Considering the months during which Group 3 and 4 MHWs are active, we compute the number of days that the MJO is active within these months using the MJO index from the Australian Government Bureau of Meteorology.

## Reporting summary

Further information on research design is available in the Nature Portfolio Reporting Summary linked to this article.

## Data availability

All data used in this study are available online. GLORYS reanalysis data is freely available at: <https://resources.marine.copernicus.eu/products>. The NOAA satellite SST at: <https://www.ncei.noaa.gov/data/sea-surface-temperature-optimum-interpolation/v2.1/access/avhrr/>, the atmospheric fields at: <https://cds.climate.copernicus.eu/cdsapp#!/dataset/reanalysis-era5-pressure-levels-monthly-means?tab=overview>, the OLR at <https://psl.noaa.gov/data/gridded/> and the ENSO Index and the MJO respectively at [https://origin.cpc.ncep.noaa.gov/products/analysis\\_monitoring/ensostuff/ONI\\_v5.php](https://origin.cpc.ncep.noaa.gov/products/analysis_monitoring/ensostuff/ONI_v5.php) and <http://www.bom.gov.au/climate/mjo/>

## Code availability

All analyses were performed using MATLAB. The library used to compute MHWs characteristics is available at <https://doi.org/10.21105/joss.01124>.

Received: 29 April 2024; Accepted: 24 September 2024;

Published online: 03 October 2024

## References

1. Von chuckmann, K. et al. Heat stored in the Earth system 1960–2020: where does the energy go?. *Earth Syst. Sci. Data* **15**, 1675–1709 (2023).
2. Oliver, E. C. et al. Marine heatwaves. *Annu. Rev. Mar. Sci.* **13**, 313–342 (2021).
3. Amaya, D. J. et al. Marine heatwaves need clear definitions so coastal communities can adapt. *Nature* **616**, 29–32 (2023).
4. Smale, D. A. et al. Marine heatwaves threaten global biodiversity and the provision of ecosystem services. *Nat. Clim. Change* **9**, 306–312 (2019).
5. Ferreira, B. P. et al. The effects of sea surface temperature anomalies on oceanic coral reef systems in the southwestern tropical Atlantic. *Coral Reefs* **32**, 441–454 (2013).
6. Rodrigues, R. R. et al. Common cause for severe droughts in South America and marine heatwaves in the South Atlantic. *Nat. Geosci.* **12**, 620–626 (2019).
7. Gianelli, I. et al. Sensitivity of fishery resources to climate change in the warm-temperate Southwest Atlantic Ocean. *Regional Environ. Change* **23**, 49 (2023).
8. Duarte, G. A. et al. Heat waves are a major threat to turbid coral reefs in Brazil. *Front. Mar. Sci.* **7**, 179 (2020).
9. Holbrook, N. J. et al. A global assessment of marine heatwaves and their drivers. *Nat. Commun.* **10**, 2624 (2019).
10. Sen Gupta, A. et al. Drivers and impacts of the most extreme marine heatwave events. *Sci. Rep.* **10**, 19359 (2020).
11. Goes, M. et al. Modulation of western South Atlantic marine heatwaves by meridional ocean heat transport. *J. Geophys. Res. Oceans* **129**, e2023JC019715 (2024).
12. Li, J., Roughan, M. & Kerr, C. Drivers of ocean warming in the western boundary currents of the Southern Hemisphere. *Nat. Clim. Change* **12**, 901–909 (2022).
13. Liu, H., Nie, X., Shi, J. & Wei, Z. Marine heatwaves and cold spells in the Brazil Overshoot show distinct sea surface temperature patterns depending on the forcing. *Commun. Earth Environ.* **5**, 102 (2024).
14. Bian, C. et al. Oceanic mesoscale eddies as crucial drivers of global marine heatwaves. *Nat. Commun.* **14**, 2970 (2023).
15. Wernberg, T. et al. An extreme climatic event alters marine ecosystem structure in a global biodiversity hotspot. *Nat. Clim. Change* **3**, 78–82 (2013).
16. Gruber, N. et al. Biogeochemical extremes and compound events in the ocean. *Nature* **600**, 395–407 (2021).
17. Costa, NatashaV. & Rodrigues, ReginaR. Future summer marine heatwaves in the western South Atlantic. *Geophys. Res. Lett.* **48**, e2021GL094509 (2021). 22.
18. Yeh, S. W. et al. ENSO atmospheric teleconnections and their response to greenhouse gas forcing. *Rev. Geophys.* **56**, 185–206 (2018).
19. Rodrigues, R. R., Campos, E. J. & Haarsma, R. The impact of ENSO on the South Atlantic subtropical dipole mode. *J. Clim.* **28**, 2691–2705 (2015).
20. Barreiro, M. Influence of ENSO and the South Atlantic Ocean on climate predictability over Southeastern South America. *Clim. Dyn.* **35**, 1493–1508 (2010).
21. McPhaden, M. J., Santoso, A., & Cai, W. Introduction to El Niño Southern Oscillation in a changing climate. El Niño Southern Oscillation in a changing climate, 1–19. <https://doi.org/10.1002/9781119548164.ch1> (2020).
22. Mo, K. C. Relationships between low-frequency variability in the Southern Hemisphere and sea surface temperature anomalies. *J. Clim.* **13**, 3599–3610 (2000).
23. Vera, C., Silvestre, G., Barros, V. & Carril, A. Differences in El Niño response over the Southern Hemisphere. *J. Clim.* **17**, 1741–1753 (2004).
24. Grimm, A. M., Pal, J. & Giorgi, F. Connection between spring conditions and peak summer monsoon rainfall in South America: Role of soil moisture, surface temperature, and topography in eastern Brazil. *J. Clim.* **20**, 5929–5945 (2007).
25. Rodrigues, R. R. & Woollings, T. Impact of atmospheric blocking on South America in austral summer. *J. Clim.* **30**, 1821–1837 (2017).
26. Gabriel, A. & Peters, D. A diagnostic study of different types of Rossby wave breaking events in the northern extratropics. *J. Meteor. Soc. Jpn.* **86**, 613–631 (2008).
27. Masato, G., Hoskins, B. J. & Woollings, T. J. Can the frequency of blocking be described by a red noise process? *J. Atmos. Sci.* **66**, 2143–2149 (2009).
28. Chapman, C. C., Monselesan, D. P., Risbey, J. S., Feng, M. & Sloyan, B. M. A large-scale view of marine heatwaves revealed by archetype analysis. *Nat. Commun.* **13**, 7843 (2022).
29. Morrow, R., Ward, M. L., Hogg, A. M., & Pasquet, S. Eddy response to Southern Ocean climate modes. *J. Geophys. Res. Oceans* **115**, <https://doi.org/10.1029/2009JC005894> (2010).
30. Manta, G. et al. The 2017 record marine heatwave in the southwestern Atlantic shelf. *Geophys. Res. Lett.* **45**, 12–449 (2018).
31. Reynolds, R. W. et al. Daily high-resolution-blended analyses for sea surface temperature. *J. Clim.* **20**, 5473–5496 (2007).
32. Hersbach, H. et al. The ERA5 global reanalysis. *Q. J. Roy. Meteorol. Soc.* **146**, 1999–2049 (2020).
33. Lellouche, J.-M. et al. Recent updates to the Copernicus Marine Service global ocean monitoring and forecasting real-time 1/12 °high-resolution system. *Ocean Sci.* **14**, 1093–1126 (2018).
34. Lellouche, J.-M. et al. Evaluation of real time and future global monitoring and forecasting systems at Mercator Ocean. *Ocean Sci. Discuss.* **9**, 1123–1185 (2013).

35. Pujol, M.-I. et al. DUACS DT2014: The new multi-mission altimeter dataset reprocessed over 20 years. *Ocean Sci.* **12**, 1067–1090 (2016).
36. Cabanes, C. et al. The CORA dataset: Validation and diagnostics of in-situ ocean temperature and salinity measurements. *Ocean Sci.* **9**, 1–18 (2013).
37. Szekely, T., Gourrion, J., Pouliquen, S., & Reverdin, G. CORA, Coriolis, Ocean Dataset for Reanalysis. SEANOE. <https://doi.org/10.17882/46219> (2016).
38. Lellouche, J.-M. et al. The Copernicus Global 1/12° Oceanic and Sea Ice GLORYS12 Reanalysis. *Front. Earth Sci.* **9**, 698876 (2021).
39. Artana, C. et al. Fronts of the Malvinas Current System: Surface and subsurface expressions revealed by satellite altimetry, Argo floats, and Mercator operational model outputs. *J. Geophys. Res. Oceans* **123**, 5261–5285 (2018). (2018).
40. Artana, C., Provost, C., Poli, L., Ferrari, R. & Lellouche, J.-M. Revisiting the Malvinas Current upper circulation and water masses using a high-resolution ocean reanalysis. *J. Geophys. Res. Oceans* **126**, e2021JC017271 (2021).
41. Poli, L. et al. Anatomy of subinertial waves along the Patagonian shelf break in a 1/12° global operational model. *J. Geophys. Res. Oceans* <https://doi.org/10.1029/2020JC016549> (2020).
42. Amaya, D. J. et al. Bottom marine heatwaves along the continental shelves of North America. *Nat. Commun.* **14**, 1038 (2023).
43. Zhang, Y. et al. Vertical structures of marine heatwaves. *Nat. Commun.* **14**, 6483 (2023).
44. Fragkopoulou, E. et al. Marine biodiversity exposed to prolonged and intense subsurface heatwaves. *Nat. Clim. Chang.* **13**, 1114–1121 (2023).
45. Hobday, A. J. et al. A hierarchical approach to defining marine heatwaves. *Prog. Oceanogr.* **141**, 227–238 (2016).
46. Zhao et al. A MATLAB toolbox to detect and analyze marine heatwaves. *J. Open Source Softw.* **4**, 1124 (2019).
47. Arthur, D., & Vassilvitskii, S. K-means++: The advantages of careful seeding. In *SODA '07: Proceedings of the eighteenth annual ACM-SIAM symposium on discrete algorithms*, 1027–1035. Retrieved from <https://theory.stanford.edu/~sergei/papers/kMeansPP-soda.pdf> (2007).

## Acknowledgements

This study is a contribution to the European Union's Horizon 2020 research and innovation programme under grant agreement No 817578 (TRIATLAS project) and the Spanish funded ProOceans project (Ministerio de Ciencia e Innovación, Proyectos de I + D + I, RETOS-PID2020-118097RB-I00). MC and CA acknowledge institutional support of the 'Severo Ochoa Centre of Excellence' accreditation (CEX2019-000928-S) to the Institute of Marine Science (ICM-CSIC). CA thanks CNES (Centre National d'Etudes Spatiales) for the constant support.

## Author contributions

C.A. and R.R. provided the conception of this study. C.A. and R.R. contributed to the design of the study. C.A. and J.F. analysed the MHW data. C.A. prepared the first draft of the manuscript. C.A., R.R. and M.C. discussed and reviewed the paper before submission.

## Competing interests

The authors declare no competing interests. R.R. is an Editorial Board Member for Communications Earth & Environment, but was not involved in the editorial review of, nor the decision to publish this article.

## Additional information

**Supplementary information** The online version contains supplementary material available at <https://doi.org/10.1038/s43247-024-01726-8>.

**Correspondence** and requests for materials should be addressed to Camila Artana.

**Peer review information** *Communications Earth & Environment* thanks Leandro Díaz and Marlos Goes for their contribution to the peer review of this work. Primary Handling Editor: Alireza Bahadori. A peer review file is available.

**Reprints and permissions information** is available at <http://www.nature.com/reprints>

**Publisher's note** Springer Nature remains neutral with regard to jurisdictional claims in published maps and institutional affiliations.

**Open Access** This article is licensed under a Creative Commons Attribution-NonCommercial-NoDerivatives 4.0 International License, which permits any non-commercial use, sharing, distribution and reproduction in any medium or format, as long as you give appropriate credit to the original author(s) and the source, provide a link to the Creative Commons licence, and indicate if you modified the licensed material. You do not have permission under this licence to share adapted material derived from this article or parts of it. The images or other third party material in this article are included in the article's Creative Commons licence, unless indicated otherwise in a credit line to the material. If material is not included in the article's Creative Commons licence and your intended use is not permitted by statutory regulation or exceeds the permitted use, you will need to obtain permission directly from the copyright holder. To view a copy of this licence, visit <http://creativecommons.org/licenses/by-nc-nd/4.0/>.

© The Author(s) 2024